

Electronic Supplementary Information (ESI)

Structural Basis for Negative Regulation of ABA Signaling by ROP11 GTPase

Chuankai Zhao^a and Diwakar Shukla^{*,a,b,c,d,e,f}

^a Department of Chemical and Biomolecular Engineering, University of Illinois at Urbana-Champaign, Urbana, IL 61801, USA. E-mail: diwakar@illinois.edu.

^b Department of Plant Biology, University of Illinois at Urbana-Champaign, Urbana, IL 61801, USA.

^c Center for Biophysics and Quantitative Biology, University of Illinois at Urbana-Champaign, Urbana, IL 61801, USA.

^d National Center for Supercomputing Applications, Urbana, IL 61801, USA.

^e NIH Center for Macromolecular Modeling and Bioinformatics, University of Illinois at Urbana-Champaign, Urbana, IL 61801, USA.

^f Beckman Institute for Advanced Science and Technology, University of Illinois at Urbana-Champaign, Urbana, IL 61801, USA.

Computational Methods

Homology modeling and structure refinement of ABI1 and active ROP11 GTPase

The initial structures of AtABI1 and the active AtROP11 GTPase were modeled via homology modeling using Swiss-Model.¹ The crystal structure of AtABI2 (PDB ID: 3UJK²) was used as the template for modeling ABI1 (sequence identity and similarity between ABI1 and ABI2: 87.17% and 57%). Two Mg²⁺ ions bound to the catalytic site of ABI1 were also included in the modeled ABI1. The crystal structure of active OsRAC1 (PDB ID: 4U5X³) was used as the template for modeling ROP11 (sequence identity and similarity between OsRAC1 and ROP11: 82.95% and 56%). The non-hydrolyzable GTP analog GMPPNP and Mg²⁺ in 4U5X were added to the modeled AtROP11 GTPase structure. GMPPNP was subsequently replaced by GTP molecule to obtain the initial homology model of active AtROP11.

Explicit solvent molecular dynamics (MD) simulations were performed to refine the modeled structures of ABI1 and ROP11. The initial structures were solvated using tleap in Ambergtools 15.⁴ Extra Na⁺ and Cl⁻ (150 mM) were added to neutralize the system and mimic physiological environment. The parameters for GTP were obtained from AMBER parameter database (<http://research.bmh.manchester.ac.uk/bryce/amber/>) and Amber ff14SB force field was used for ABI1 and ROP11. The AMBER force field parameters for monovalent and divalent ions available in AMBER 18 software⁴ were used. The system was subjected to 10000 steps of minimization and subsequent 1 ns equilibration at 300 K. Production simulations were launched from the equilibrated configuration and run for 100 ns. The simulations were run in isothermal-isobaric (300 K, 1 atm) ensemble using an integration time step of 2 fs. The temperature was controlled using Langevin dynamics⁵ with the collision frequency of 2 ps⁻¹ and the pressure was maintained using Monte Carlo barostat. Periodic boundary condition was applied in all MD simulations. The particle-mesh Ewald method was used to treat the electrostatic interactions, along with a 10 Å cutoff distance for van der Waals interactions.⁶ The SHAKE algorithm⁷ was applied to constrain the length of covalent bonds involving hydrogen atoms.

Coarse grained (CG) molecular dynamics (MD) simulations of ROP11 and ABI1 association

The atomic structures of ABI1 and ROP11 obtained after MD refinement were used to construct CG structural models and run CG MD simulations using Martini force field.^{8,9} For ROP11, Q66L mutation was performed using Pymol to mimic a constitutively active ROP11 (CA-ROP11).^{10,11} In such way, GTP and Mg²⁺ were not included in CA-ROP11 structure. The script Martinize.py (version 2.6, <http://cgmartini.nl/index.php/tools2/proteins-and-bilayers>) was used to convert the atomic structures of CA-ROP11 and ABI1 to CG bead models and also generate the Martini topology files in Gromacs format. In short, CG bead models were produced according to 4 heavy atoms to 1 bead mapping and different types of beads were defined to represent different subgroup of atoms. Elastic network was applied in combination with Martini model to conserve secondary, tertiary and quaternary structures without sacrificing realistic dynamics of the proteins.¹² *ElNeDyn* network was used to generate the topology files of the proteins.¹²

Next, the CG structural models of ABI1 and CA-ROP11 were randomly placed far away from each other to generate 50 configurations of ABI1/CA-ROP11 complexes, with their center-of-mass distance at least 25 Å. The 50 complex structures were solvated using an equilibrated CG water box via Gromacs solvate command. Also, 30 CG Na⁺ and 31 Cl⁻ beads were added to neutralize the system. The system was subjected to 0.2 ns equilibration in Gromacs.¹³ Production simulations were launched from the equilibrated configurations. Adaptive sampling approach was used to efficiently sampling the association process between ABI1 and CA-ROP11.¹⁴ In the initial round of simulations, the simulations started from 50 configurations. In the next rounds of simulations, the previously sampled complex conformations were clustered into a certain number of states. A portion of the states with the lowest populations were selected to start new simulations, with the initial velocities randomly assigned according to Boltzmann distribution.

The CG MD simulations were performed with Gromacs 2019¹³ in isothermal-isobaric (300 K, 1 atm) ensemble using an integration time step of 20 fs. The temperature control was achieved with the velocity rescale (V-rescale) thermostat using a coupling constant of the order of 1 ps. The pressure control was realized with the Parrinello-Rahman barostat, with a coupling constant of 16 ps and compressibility of 3*10⁻⁴ bar⁻¹. Periodic boundary conditions were applied in all MD simulations. The particle-mesh Ewald method was used to treat the electrostatic interactions, along with a 11

Å cutoff distance for van der Waals interactions.⁶ In total, 5 rounds of adaptive sampling simulations were performed, leading to an aggregate of 10.05 ms simulations (Table S2).

Markov state model analysis of simulation data on CA-ROP11 and ABI1 association

Markov state model (MSM) was used to analyze the conformational ensemble of ABI1 and CA-ROP11 resulted from CG MD simulations. MSM is a powerful method to analyze large-scale MD simulation data on biomolecules.^{15,16} Generally, MSMs characterize biomolecule conformation ensemble as discrete conformational states and inter-state transition probabilities between them.^{15,16} The equilibrium probabilities of individual states can then be estimated from MSM, allowing us to gain insights into the probable configurations of ABI1/CA-ROP11 complex.

The discretization of conformational space was achieved by identifying a set of structural features to represent individual configurations and then clustering these configurations into a certain number of states. In total, 6 structural metrics were calculated to differentiate various configurations, including the center-of-mass distance between ABI1 and CA-ROP11 as well as 5 angles or dihedral angles that describe the relative orientation and position of ABI1 and CA-ROP11 (Fig. S2). Time-lagged independent component analysis was performed to identify several slowest degrees of freedom (tICs) resulted from linear combination of the original metrics.¹⁷ K-means clustering were then performed on the identified slowest motions to cluster the CG configurations into a certain number of states. MSMs were then constructed based on the clustering results. The matrix of transition probabilities was determined with a lag time τ using maximum likelihood approximation. The optimal lag time (τ) was chosen based on the convergence of the implied timescales of MSMs and the number of clusters (N) as well as the number of tICs (M) were optimized via cross validation ranked by the variational GMRQ objective function (Fig. S3).¹⁸ All MSMs were constructed using the MSMBuilder 3.4¹⁹ and the MSM hyperparameters were optimized using the Osprey software.²⁰ The final MSM hyperparameters were 600 clusters, 4 tICs, and 800 ns lag time.

All atom MD simulations for structural refinement of 23 candidate complex structures

The 25 MSM states with the largest equilibrium populations were converted back to atomic structural models using the script backward.py (<http://www.cgmartini.nl/index.php/downloads/tools/240-backward>).²¹ The backward mapping was performed using the wrapper initram.sh, which calls backward.py and subsequently relaxes the resulting structure through energy minimization and molecular dynamics based relaxation. Due to the possible inaccuracy of structural models from backward mapping, we aligned the atomic structures of ABI1 and GTP-bound ROP11 to these 25 complexes and sought to use MD simulations to further refine these candidate complex structures. We observed that 3 states among the top 25 states were similar so that we merged the 3 states, resulting in 23 states to be optimized.

The atomic structures of the 23 candidate complexes were solvated with water molecules and counterions. Two parallel MD simulations were launched from the equilibrated configurations with Amber 18⁴ and each was run for 240 ns to relax the atomic structures. The same set of force field parameters and simulation protocols as in the step of structural refinement of homology models were used to run these simulations. After the simulations were finished, the root mean square deviation of these complex structures and the center-of-mass distance between ABI1 and ROP11 were calculated to characterize the relative stability of the 23 complex structures. Based on these simulation data, we further excluded 10 complex structures, leading to 13 remaining candidate complex structures.

Replica exchange umbrella sampling MD simulations for potential of mean force calculations

To further differentiate the 13 candidate complex structures, we sought to calculate potential of mean force (PMF) for separating ABI1 and ROP11 in these different complex structures. The PMFs were determined by separating two proteins in the presence of a series of conformational, positional and orientational restraints and then performing replica exchange umbrella sampling (REUS) MD simulations to estimate the conformational probability distribution with respect to separation distance r . By applying these restraints, it effectively reduce the configuration entropy of complex and accelerate the convergence of separation PMF. In total, there were 7 harmonic restraints applied during separation, including two relating to conformational changes in ABI1 and ROP11 (denoted by subscripts B_{ABI1} , B_{ROP11}) and 5

relating to relative position and orientation between two proteins. The conformational restraints acting on heavy-atom RMSD of the backbone in each protein (B_{ABI1} , B_{ROP11}) restrict protein structural fluctuations and deviations from the starting associate state. Three angular restraints acting on the relative orientation of two proteins (denoted by subscript o , including Θ , Φ , Ψ) and two on the relative position (denoted by a , including ϕ , θ) limit the configuration space when two proteins are separated.

REUS MD simulations²² were used to calculate the separation PMFs of the 13 candidate complex structures. REUS simulations were performed using NAMD 2.13 software²³. The complexes were solvated with a sufficiently large water box which encompasses both ABI1 and ROP11 when fully separated. After 20000 steps energy minimization, each system was equilibrated in NPT ensemble for 1 ns. An additional 200 ps simulation for each system was performed to measure the average values of all restrained CVs in the associated state. Next, steered MD simulations were performed to slowly increase the center-of-mass distance between ABI1 and ROP11 (r) by 15 Å over 8 ns, in order to generate starting structures for REUS MD simulations. From the trajectory, 31 structures with r evenly spaced between the minimum and the maximum distances were chosen as the starting structures for REUS MD simulations (31 windows, 0.5 Å/window). The starting structure in each umbrella window was equilibrated for 1 ns and then each replica was run for 8 ns. The force constants for the restrained CVs were given in Table S3. The separation PMF was estimated using the multistate Bennett acceptance ratio (MBAR) method with pymbar python package²⁴. The trajectories from simulations were sorted and subsampled to ensure uncorrelated samples for estimating PMF. According the separation PMFs, we identified 3 candidate complex structures which show relative higher stability as compared to other states.

Replica exchange umbrella sampling MD simulations for standard binding free energy calculations

We sought to determine the absolute standard binding free energy (ΔG_{bind}^o) of the 3 candidate complex structures. The PMF-based approach to determining ΔG_{bind}^o was developed by prior studies.^{25,26,27} The detailed theory of this method was thoroughly described in our previous work.²⁸ Integration of the separation PMF contributes to the major component of ΔG_{bind}^o . Next, the contributions of adding the conformational and angular restraints on the associated state and removing them from the fully dissociated state to ΔG_{bind}^o were also computed and then subtracted from the free energy component resulting from separation PMF. Given the equilibrium association constant, ΔG_{bind}^o is given by

$$\Delta G_{bind}^o = -\beta^{-1} \ln(K_{eq} C^o) \quad (1)$$

where β is the reciprocal of the product of gas constant and temperature, and C^o is standard concentration of 1 M, which is $1/1661 \text{ \AA}^3$. K_{eq} can be expressed as in equation 2.

$$K_{eq} = S^* I^* e^{-\beta[(G_{B_{1,c}}^{bulk} - G_{B_{1,c}}^{site}) + (G_{B_{2,c}}^{bulk} - G_{B_{2,c}}^{site})]} * e^{-\beta[(G_o^{bulk} - G_o^{site}) - G_a^{site}]} \quad (2)$$

The term S^* addresses the removal of positional restraints (θ , ϕ) on one protein, which is separated from the other protein along r instead of free diffusion. S^* is given by

$$S^* = r^{*2} \int_0^\pi d\theta \sin\theta \int_0^{2\pi} d\phi e^{-\beta u_a(\theta, \phi)} \quad (3)$$

where r^* is a point far from the binding site and $u_a = u_\theta + u_\phi$. The term I^* is given by

$$I^* = \int_{site} dr e^{-\beta[W(r) - W(r^*)]} \quad (4)$$

which includes the contribution from the separation PMF $W(r)$.

The exponential terms in equation 2 are related to adding the restraints on the associated state (denoted by site) and removing the restraints from the dissociated state (denoted by bulk). These terms can be determined by calculating a series of PMFs for individual restraints and integrating over the PMFs. REUS MD simulations along the restrained CVs were performed to calculate the free energy contributions of adding those restraints to the associated state and removing them from the dissociated state. To generate a wide range of starting structures for each restrained CV, we performed 6 ns temperature-accelerated MD simulations, coupling with the respective CV to a dummy particle experiencing a temperature of 2500 K. The starting structures for REUS windows were chosen from the accelerated MD trajectory, with a window size of 0.05 Å for conformational restraints and 1° for angular restraints. Each replica was equilibrated for 1 ns and then run for 8 ns. The force constants used were 1000 kcal·mol⁻¹·Å⁻² for RMSD restraints and 2.5 kcal·mol⁻¹·°⁻² for angular restraints. The PMFs were determined using MBAR. For some of the RMSD restraints, we performed additional targeted MD simulations and umbrella sampling simulations to expand the ranges of PMFs and ensure the convergence of PMFs. Given the PMFs, the contributions of adding and removing restraints to ΔG_{bind}^o can be calculated via numerical computations. Please refer to our previous work for more details.²⁸

Residue-residue Interaction energies and protein energy network analysis

To identify the critical residue pairs for intermolecular interaction between ABI1 and ROP11, we performed residue-residue interaction energies and protein energy network analysis on MD trajectories using gRINN version 1.1.0.hf1 (<https://grinn.readthedocs.io/en/latest/>).²⁹ gRINN computes pairwise residue non-bonded interaction energies by repeatedly calling the MD simulation engine in GROMACS 2019¹³. Default values of 60% percent cutoff and 20 Å filtering distance cutoff were used, which implied that only the residue pairs between ABI1 and ROP11 whose center-of-mass distances are less than 20 Å in at least 60% of trajectory frames will be included in the calculation. In total, 250 frames of all-atom MD trajectories for the state 160 and the state 240 were used for the calculations. Residue pairwise correlations and protein energy network (PEN) were also computed using gRINN. Protein energy network (PEN) was constructed by considering individual residues as nodes and mean interaction energies between residue pairs as the ‘weight’ for the edges that connect these residue nodes. Using PEN, node-based network metrics including degree and betweenness-centralities were obtained to assess the importance of each residue in terms of protein stability.

Table S1. Overview of the computational simulations and analysis method performed in this study.

step	system	method	force field	software	#atoms/beads	size (Å ³)	ensemble	simulation time
1	ROP11 active structure	homology modeling	-	Swiss-Model	-	-	-	-
2	ROP11 structure refinement	all atom MD	Amber ff14SB	Amber 18	35,714 atoms	67*67*81	NPT	100 ns
3	CA-ROP11 (Q66L)-ABI1 association	adaptive sampling, coarse grained MD	Martini	Gromacs 2019	~22,000 beads	~140*140*140	NPT	10.05 ms
4	analysis of complex ensemble	Markov state model	-	MdTraj, MSMBuilder	-	-	-	-
5	structural refinement of top 23 candidate complexes	all atom MD	Amber ff14SB	Amber 18	~170,000 atoms	~120*120*120	NPT	240*23*2 ns
6	PMF and binding free energy calculations	REUS MD	Amber ff14SB	NAMD 2.13	~95,000 atoms	~80*95*138	NPT	>=8 ns/window
7	Residue interaction energies and protein energy network analysis	-	Amber ff14SB	gRINN	-	-	-	-

Table S2. Summary of the adaptive coarse grained MD simulations of the association process between ABI1 and CA-ROP11 (Q66L). In the initial round of simulations, the simulations started from 50 configurations where ROP11 and ABI1 were randomly placed far away from each other. In the next rounds of simulations, the previously sampled complex conformations were clustered into a certain number of states. A portion of the states with the lowest populations were selected to start new simulations, with the initial velocities randomly assigned according to Boltzmann distribution.

Round	Parallel simulations	Simulation time (μ s)	Aggregate (ms)
1	50	21	1.05
2	100	10	1
3	200	10	2
4	200	10	2
5	400	10	4
Total simulation time: ~10.05 milliseconds			

Table S3. The restrained CVs and the corresponding force constants used in REUS MD simulations on the separation of candidate ROP11-ABI1 complex structures.

CV	k_{force}
$B_{1,c}$	$25 \text{ kcal}\cdot\text{mol}^{-1}\cdot\text{\AA}^{-2}$
$B_{2,c}$	$25 \text{ kcal}\cdot\text{mol}^{-1}\cdot\text{\AA}^{-2}$
Θ	$0.1 \text{ kcal}\cdot\text{mol}^{-1}\cdot\text{o}^{-2}$
Φ	$0.1 \text{ kcal}\cdot\text{mol}^{-1}\cdot\text{o}^{-2}$
ψ	$0.1 \text{ kcal}\cdot\text{mol}^{-1}\cdot\text{o}^{-2}$
ϕ	$0.1 \text{ kcal}\cdot\text{mol}^{-1}\cdot\text{o}^{-2}$
θ	$0.1 \text{ kcal}\cdot\text{mol}^{-1}\cdot\text{o}^{-2}$
r	$25 \text{ kcal}\cdot\text{mol}^{-1}\cdot\text{\AA}^{-2}$

Table S4. The 20 residue-residue pairs between ABI1 and ROP11 with the highest mean interaction energy (MIE) in state 160. MIE was calculated from a 500-ns all-atom MD trajectory using gRINN.²⁹

ROP11 residues	ABI1 residues	MIE (kcal/mol)
K32	D278	-22.49
K163	Q299	-18.18
K32	D351	-16.15
K32	W350	-15.79
D36	H179	-14.58
T29	R409	-11.13
D127	W300	-9.82
T35	R304	-9.20
K32	D282	-8.19
D36	R137	-8.00
K32	D261	-7.74
V41	K412	-7.39
D36	R304	-7.19
K32	M353	-7.15
K163	D282	-5.92
N44	Q408	-4.40
D123	W300	-4.33
Y37	D347	-3.99
Y37	R137	-3.91
T35	D351	-3.57

Table S5. The 20 residue-residue pairs between ABI1 and ROP11 with the highest mean interaction energy (MIE) in state 240. MIE was calculated from a 250-ns all-atom MD trajectory using gRINN.²⁹

ROP11 residues	ABI1 residues	MIE (kcal/mol)
D127	R189	-65.05
K128	E190	-32.65
D16	K372	-28.93
D133	K391	-20.86
D68	K371	-13.16
H129	E190	-12.78
H134	K391	-11.79
V90	K391	-6.47
D133	S146	-5.66
D68	K372	-5.25
G65	K372	-4.27
P135	K391	-3.92
Y130	K391	-2.88
S88	E400	-2.72
K128	N186	-2.50
Y37	Q408	-2.43
D133	Y129	-2.4
D127	A144	-2.11
D133	A144	-2.05
L124	R189	-1.72

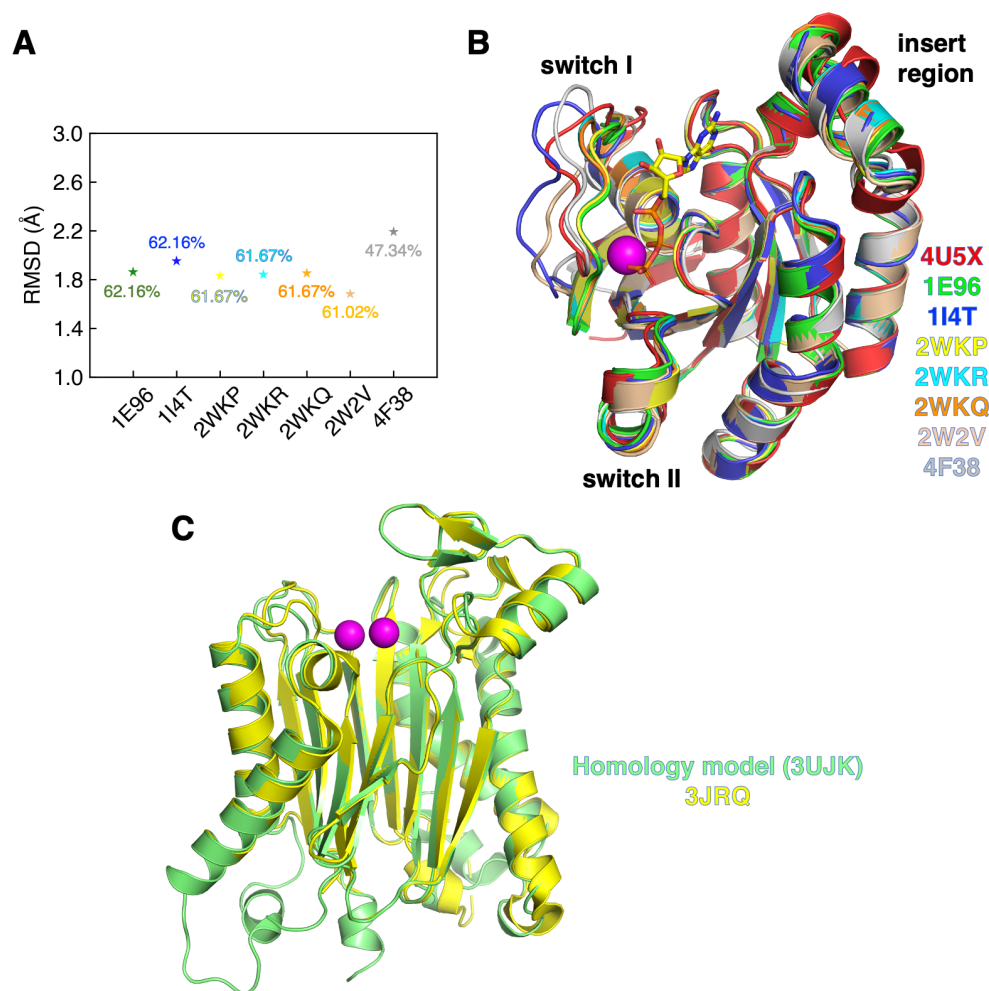


Fig. S1. Evaluation of the quality of homology models of AtROP11 and AtABI1. (A) Root mean square deviation between the crystal structures of OsRAC1 (the GTPase template for ROP11, PDB ID: 4U5X) and seven active GTPases with varying degrees of sequence identity to OsRAC1 (PDB IDs: 1E96, 1I4T, 2WKP, 2WKR, 2WKQ, 2W2V, and 4F38) are generally smaller than 2.2 Å. (B) The crystal structures of OsRAC1 and seven GTPases share the same fold, and the switch II and the insert region are highly conserved while the switch I region demonstrates slight variation. As the sequence identity between AtROP11 and OsRAC1 is 82.95%, the homology model of ROP11 using OsRAC1 as the template is of good quality. (C) Structural comparison between the homology model of ABI1 (template PDB ID: 3UJK, lime) and the crystal structure of ABI1 (PDB ID: 3JRQ, yellow). The RMSD between two structures is 1.42 Å.

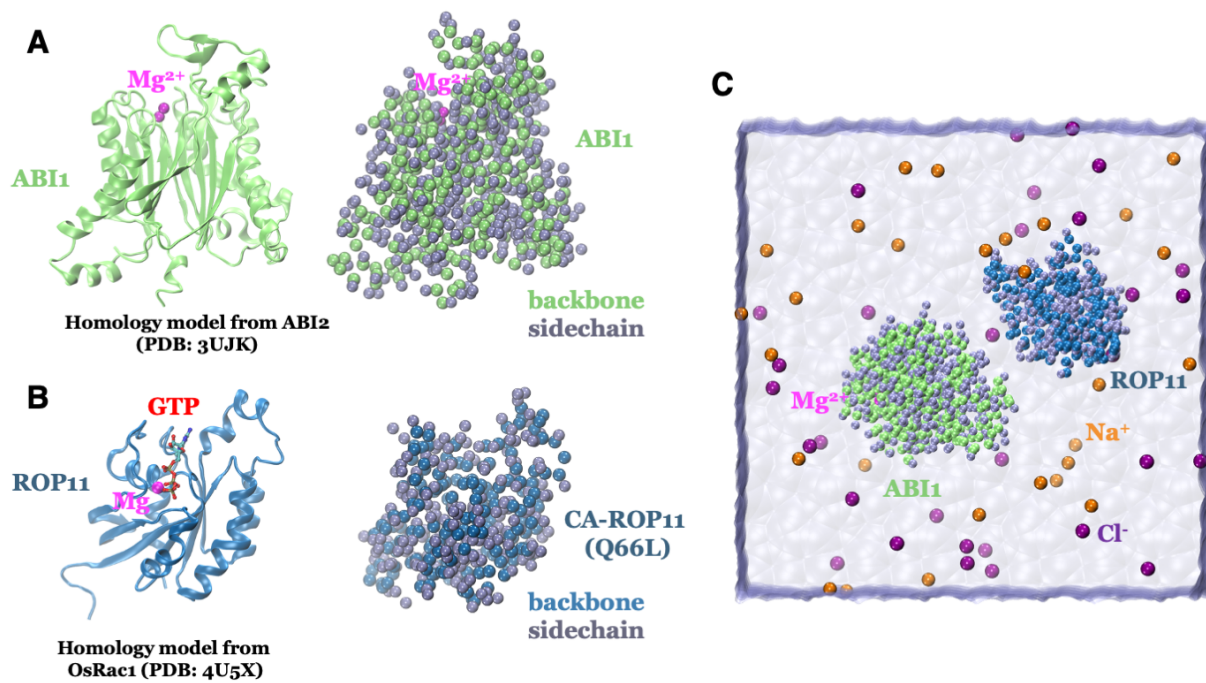


Fig. S2. Schematic of CG models of ABI1 and CA-ROP11 and CG MD simulations. Atomic (left) and CG bead (right) representations of (A) ABI1 and (B) CA-ROP11. Backbone beads of ABI1 and CA-ROP11 are shown in lime and blue, respectively. Sidechain beads are shown in purple. (C) A representative view of explicit solvent and periodic CG MD simulation box.

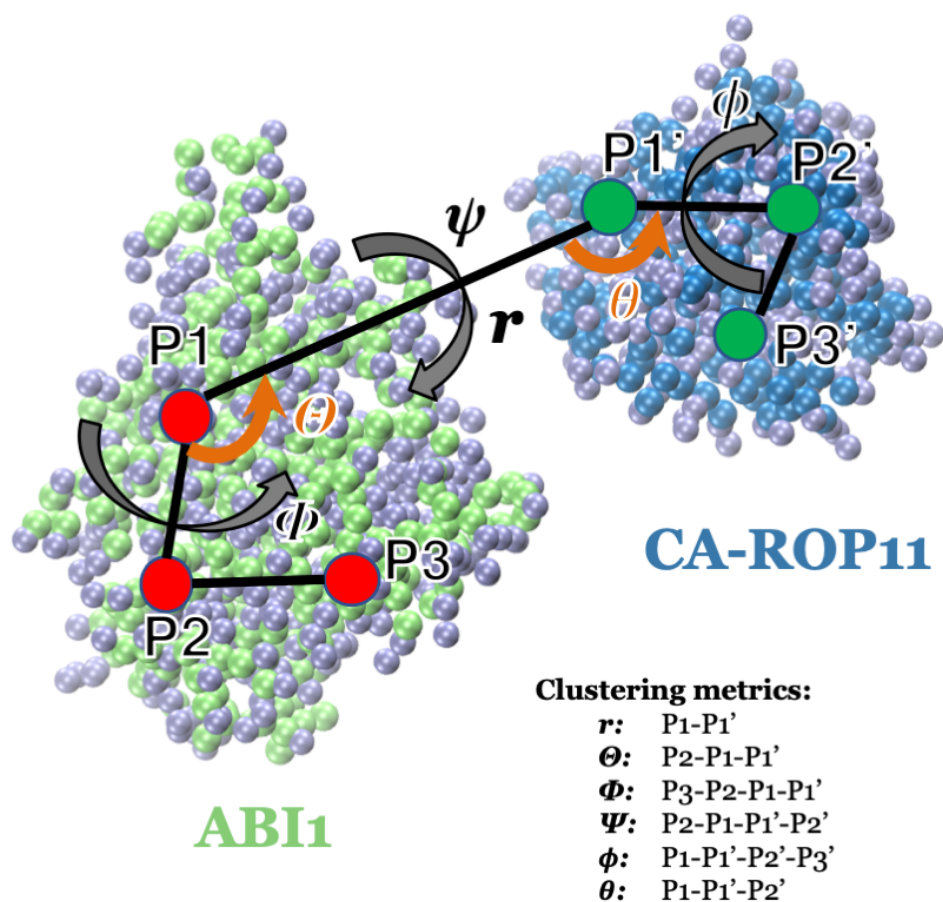


Fig. S3. Schematic of structural features used for clustering ABI1/CA-ROP11 complex conformations. In both ABI1 and ROP11, three points (P1, P2 and P3 in ABI1, P1', P2' and P3' in CA-ROP11) were defined as the centers of mass of groups of atoms. The distance between P1 and P1' characterizes the distance between ABI1 and CA-ROP11. The angles Θ (P2-P1-P1') and θ (P1-P1'-P2') as well as the dihedral angles Φ (P3-P2-P1-P1'), ϕ (P1-P1'-P2'-P3') and ψ (P2-P1-P1'-P2') together characterizes the relative position and orientation between ABI1 and CA-ROP11.

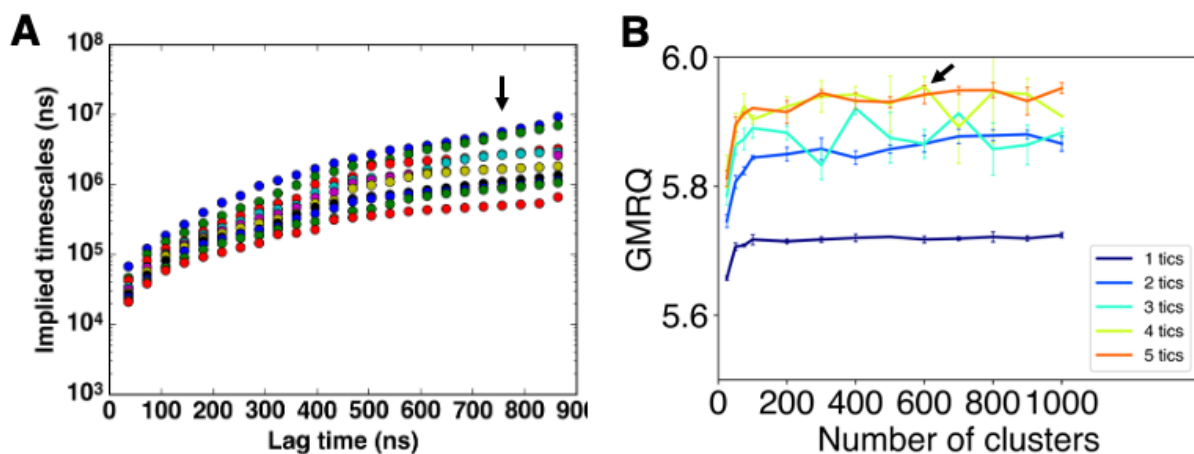


Fig. S4. Hyperparameter selection for construction of Markov state models of ABI1/CA-ROP11 association. (A) Convergence of the implied timescales of the slowest processes captured by MSMs with respect to increasing lag times. A lag time of 800 ns was used for the final MSM. (B) GMRQ scores for ranking how well MSMs with various numbers of clusters and tICs capture the slowest processes of ABI1 and ROP11 association. Based on the GMRQ scores, the set of parameters (600 clusters and 4 tICs) was chosen to construct the final MSM.

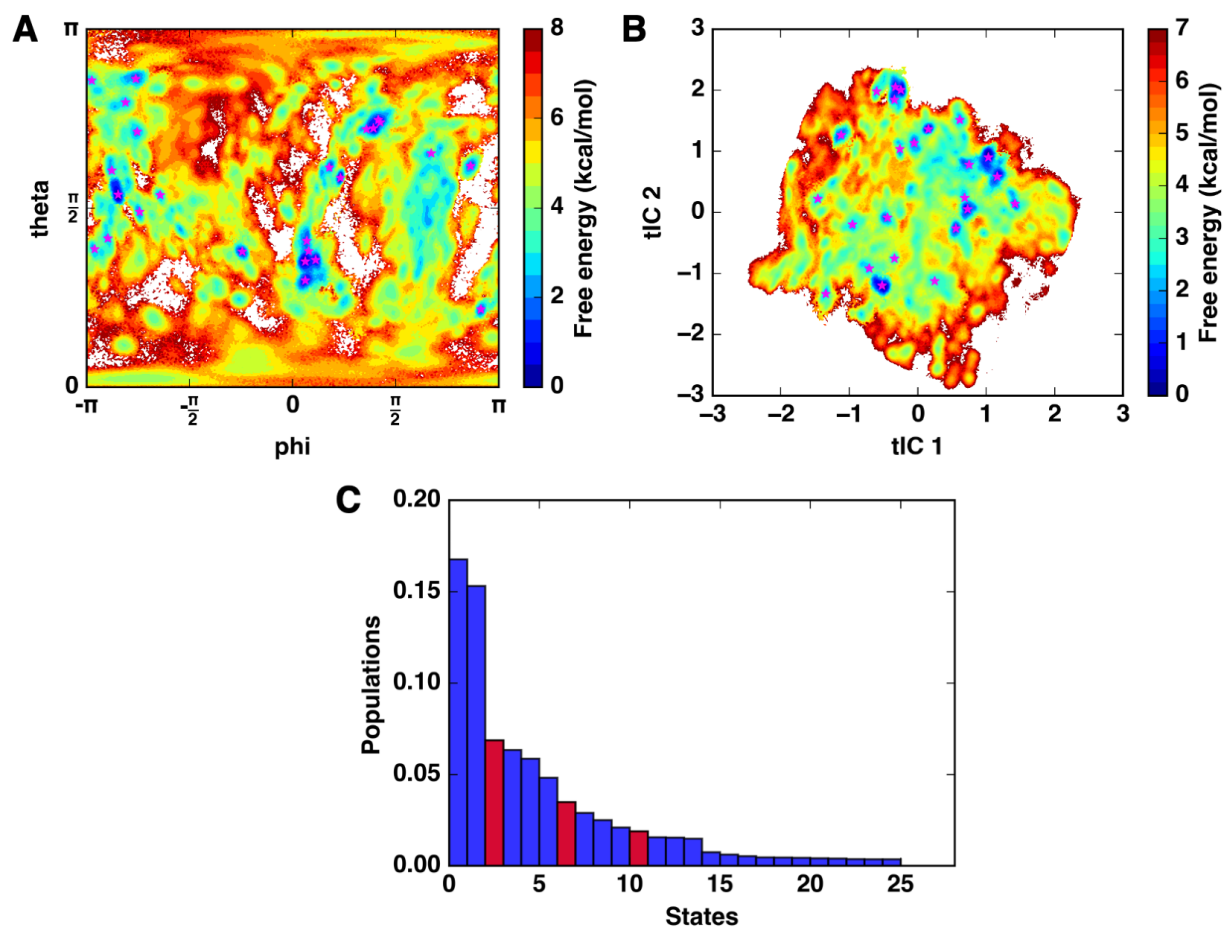


Fig. S5. ABI1-ROP11 conformational ensemble sampled from CG MD simulations. Conformational free energy landscape projected onto (A) ϕ and θ and (B) the two slowest degrees of freedom (tIC1, tIC2) resulted from time-lagged independent component analysis of the clustering metrics. Top 25 most populated MSM states are mapped onto the free energy landscape according to their tIC1 and tIC2 values. (C) The equilibrium populations of top 25 states ranked by descending order. Sum of the populations of the top 25 states is greater than 80% of the total populations. The three states with similar complex structures are highlighted in red.

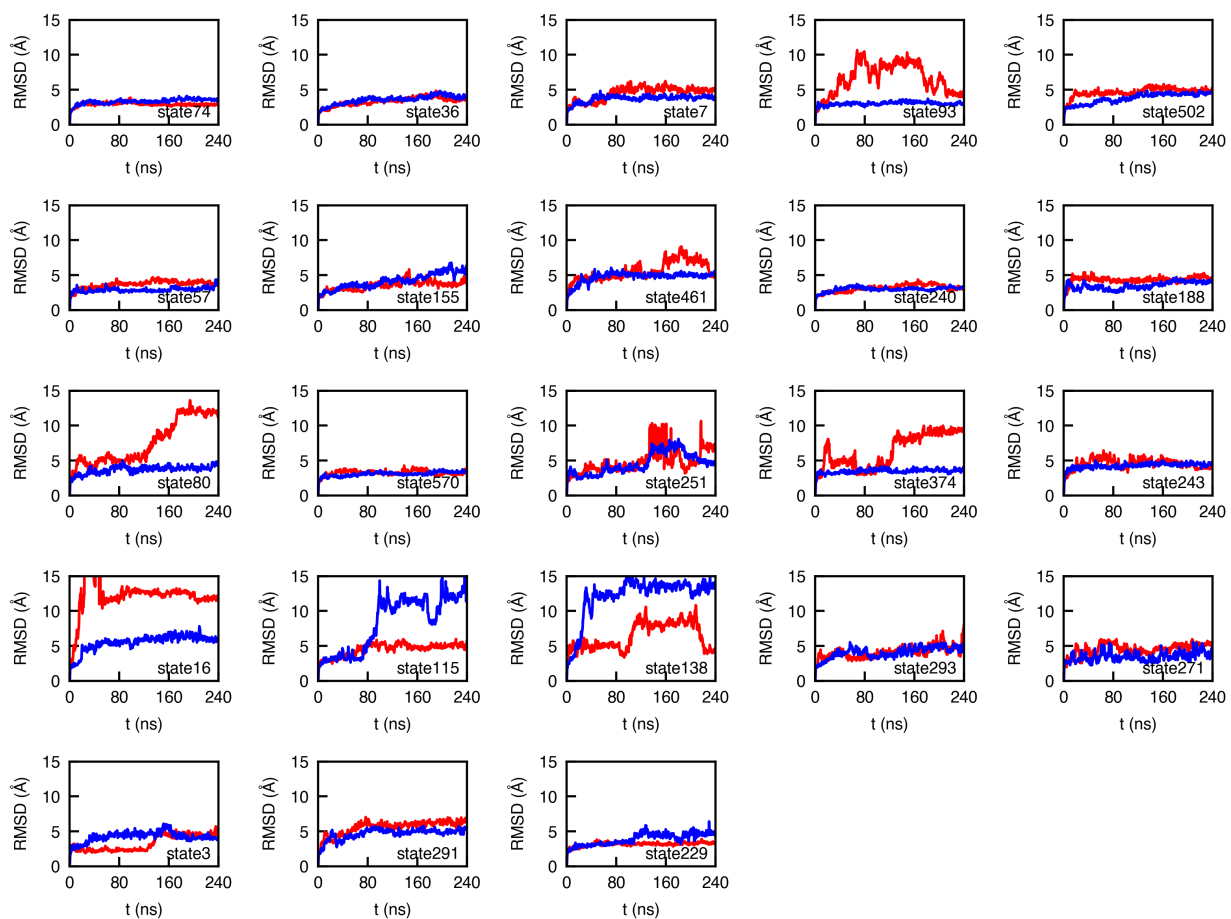


Fig. S6. Plots of RMSD, with respect to the first frame of each trajectory, for the 23 candidate complex structures during 240 ns all atom MD simulations.

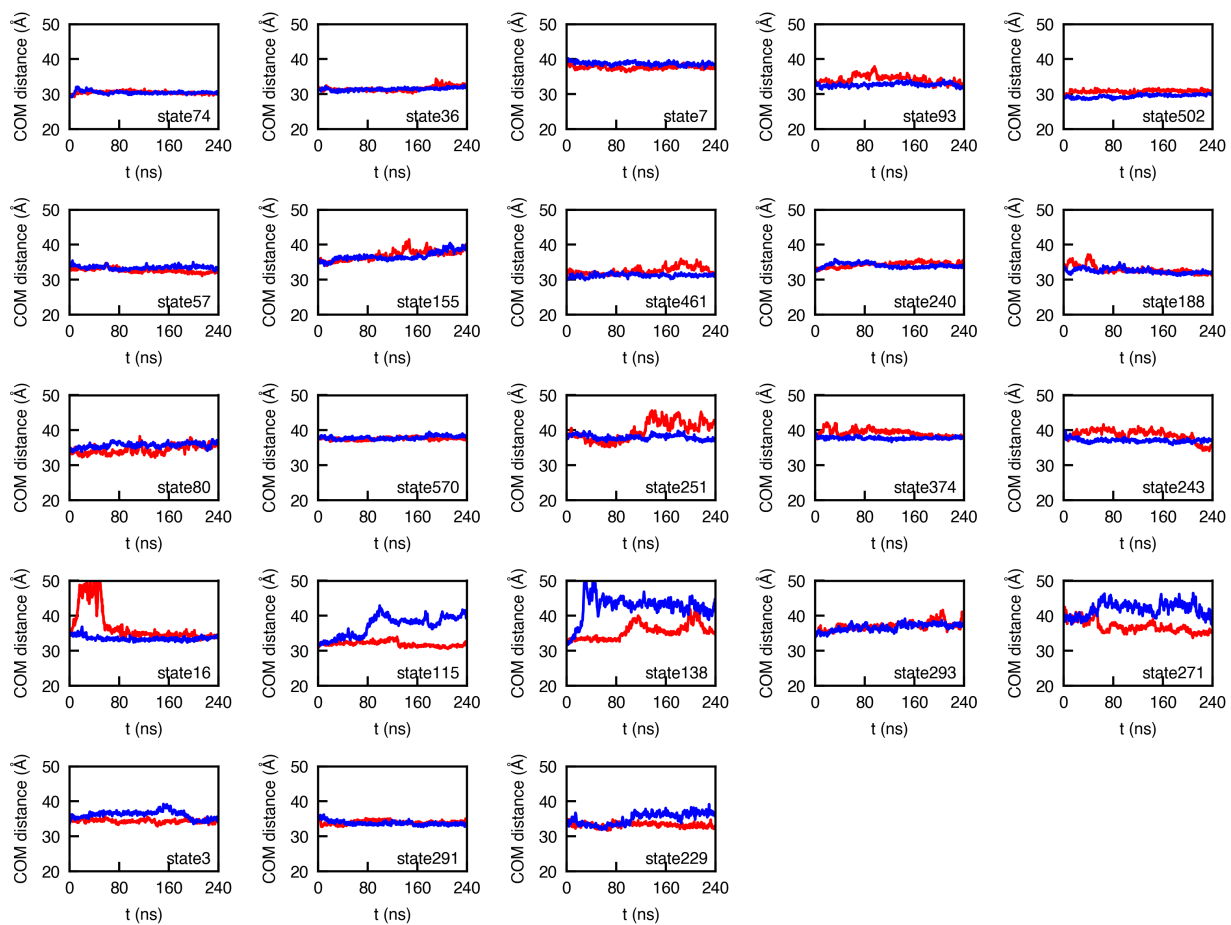


Fig. S7. Plots of center-of-mass distance for the 23 candidate complex structures during 240 ns all atom MD simulations.

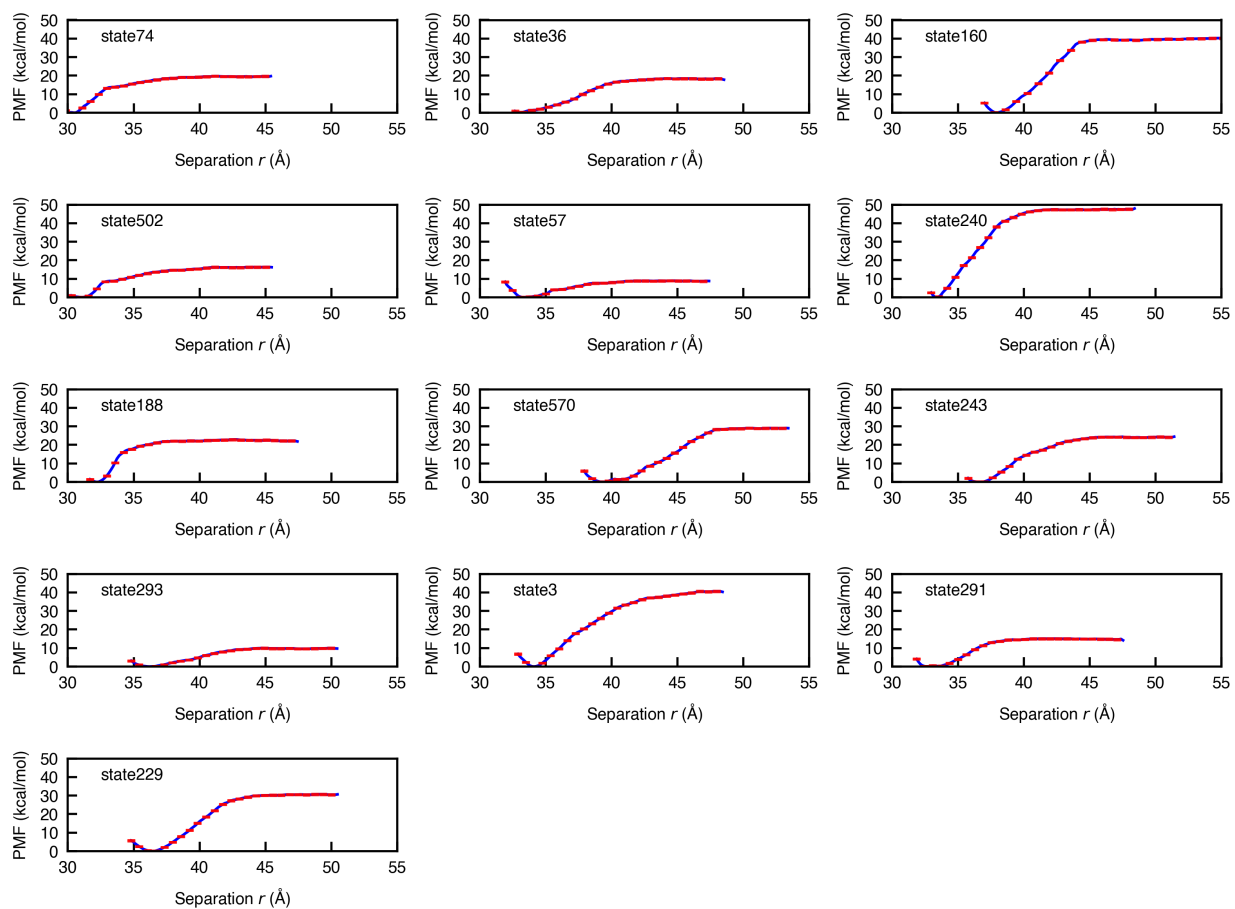


Fig. S8. Potential of mean force profiles for separating the top 13 candidate complex structures in the presence of conformational and angular restraints. The error bars on the PMFs are shown. The PMF depths indicate relative stability of the 13 candidate complex structures.

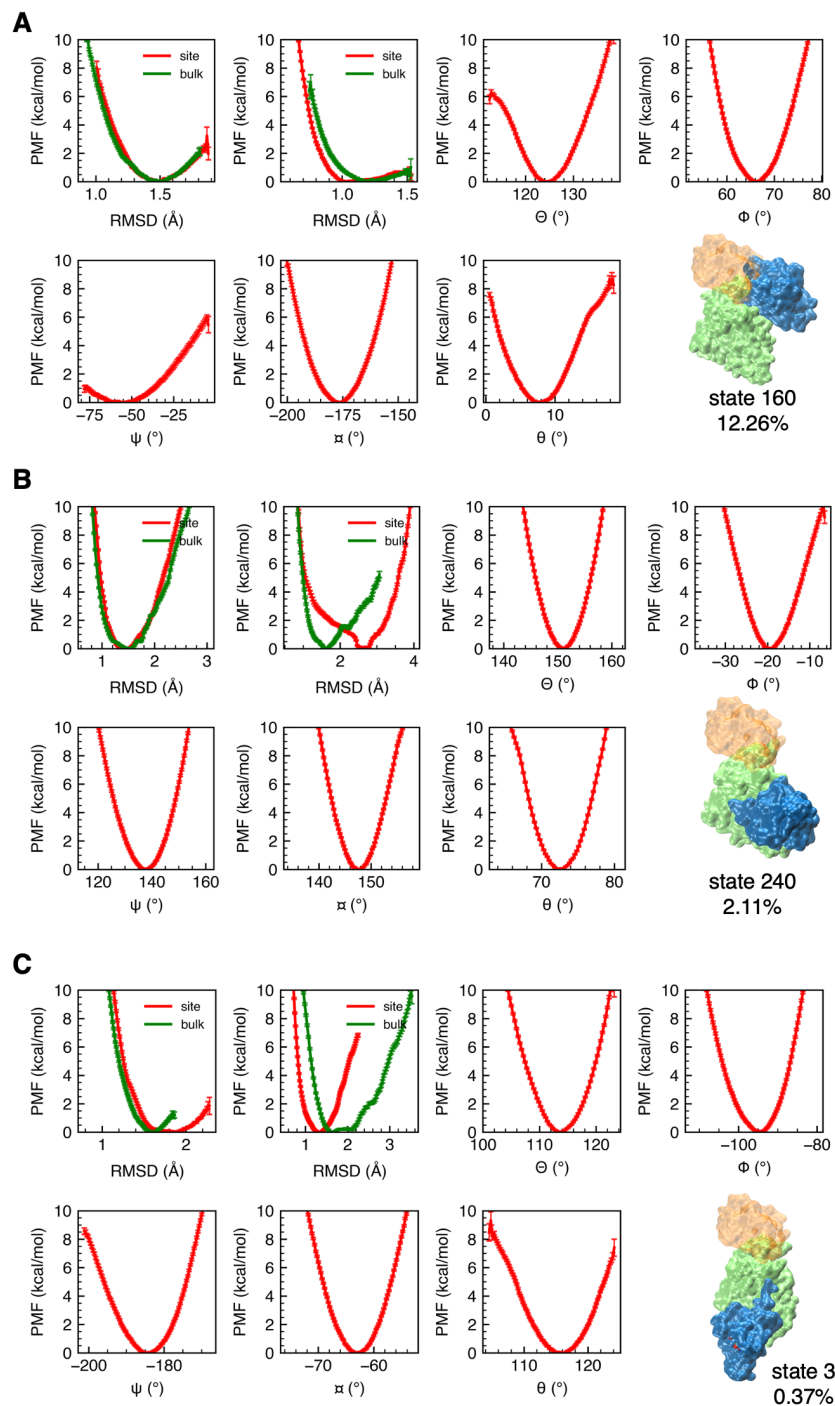


Fig. S9. Individual PMFs for all restraint components on (A) state 160, (B) state 240, and (C) state 3. Plots for the conformational and angular restraints $B_{ABI1,c}^{site}$ and $B_{ABI1,c}^{bulk}$, $B_{ROP11,c}^{site}$ and $B_{ROP11,c}^{bulk}$, Θ , Φ , ψ , ϕ and θ are shown along with the error bars on the PMFs.

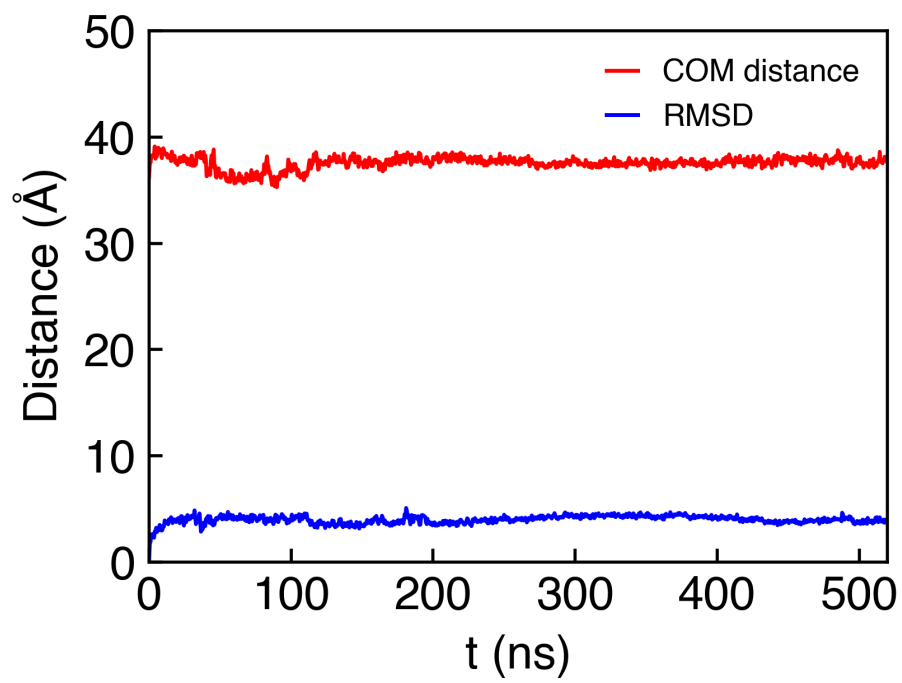


Fig. S10. The predicted complex structure (state 160) remains highly stable within 500 ns simulations. RMSD from the initial frame and the center-of-mass distance between ABI1 and ROP11 are plotted with respect to simulation time.

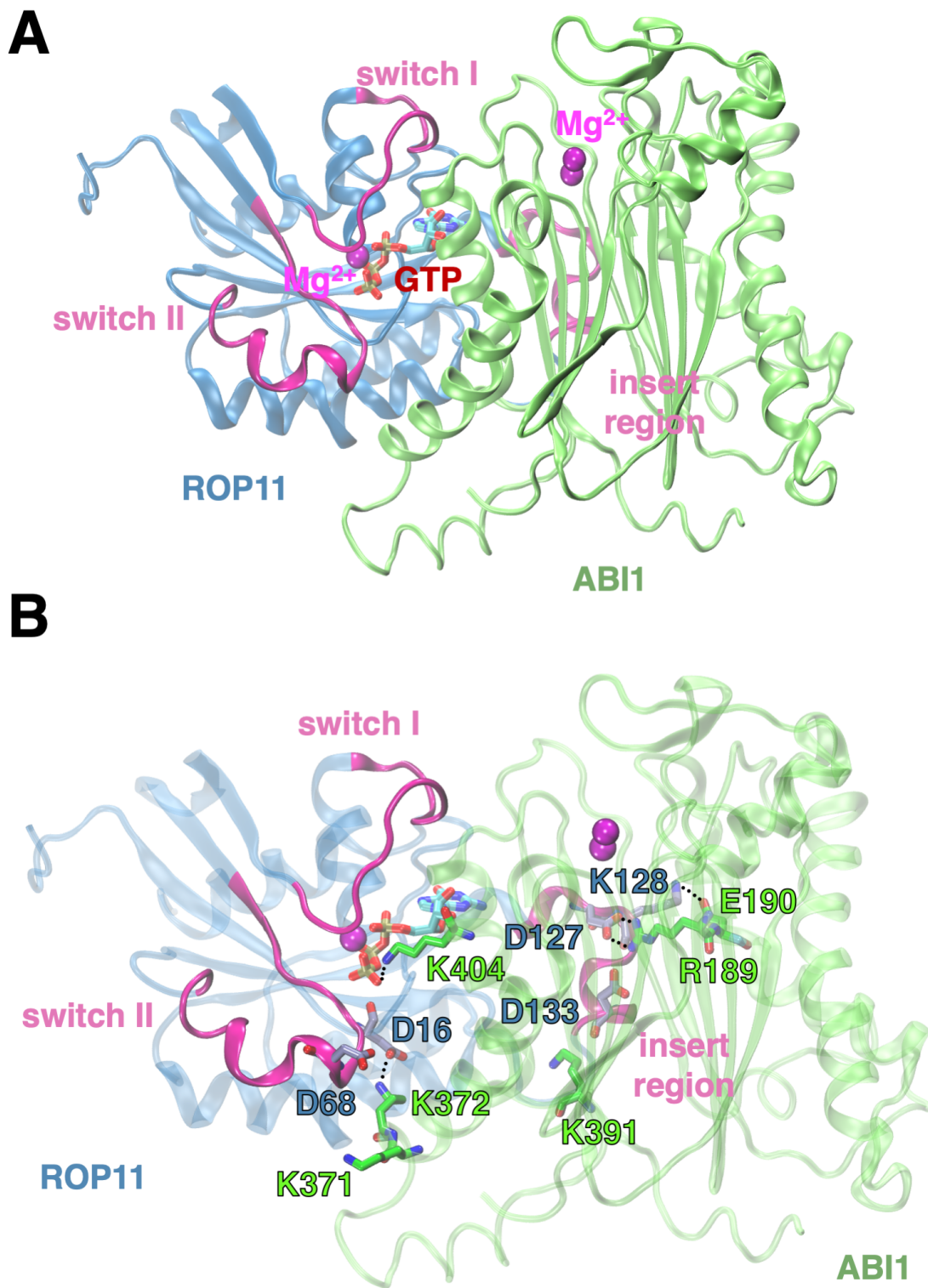


Fig. S11. (A) The candidate complex structure of the state 240 and (B) the molecular interactions at ABI1-ROP11 interface in the state 240. The state 240 is stabilized via the electrostatic interaction between both the charged residue pairs in ABI1 and ROP11 and GTP and K404 in ABI1.

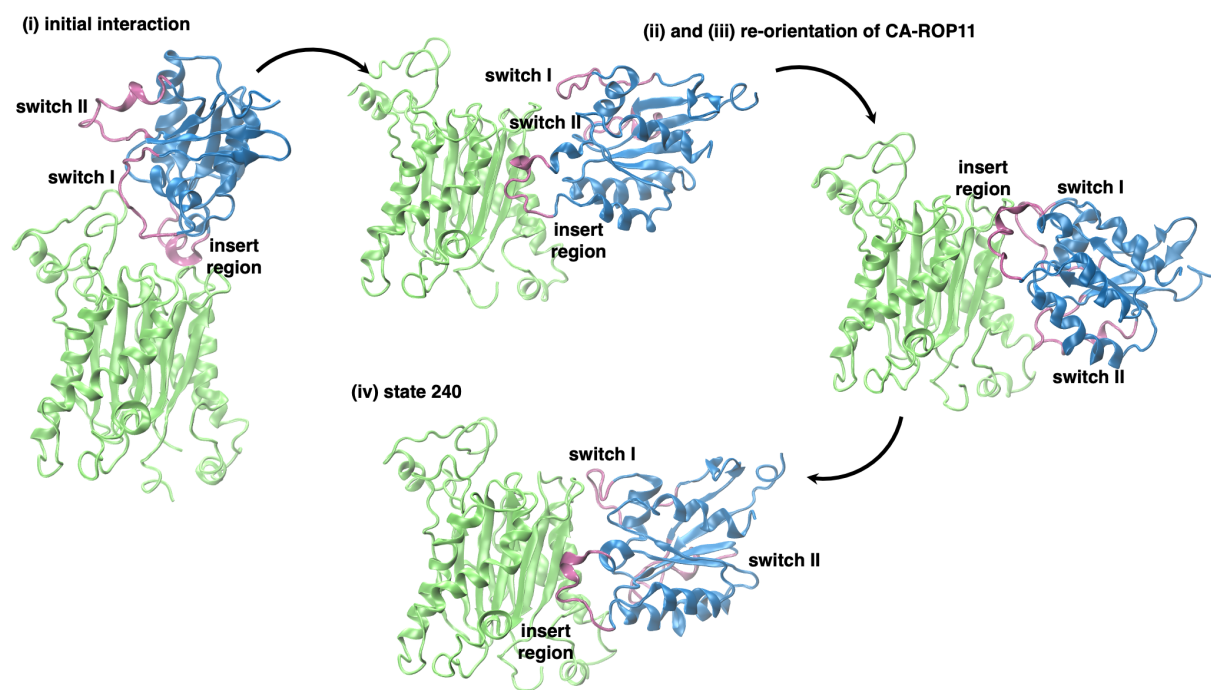


Fig. S12. The association pathway between ABI1 and CA-ROP11 to form state 240 predicted from CG MD simulations. The initial interaction between ABI1 and CA-ROP11 is mediated by the charged residues in ABI1 and the insert region of CA-ROP11. Next, CA-ROP11 adapts the orientation to rotate around ABI1 and assumes the pose in state 240. This transition pathway was generated by performing transition path theory analysis on the MSM from CG MD simulations.

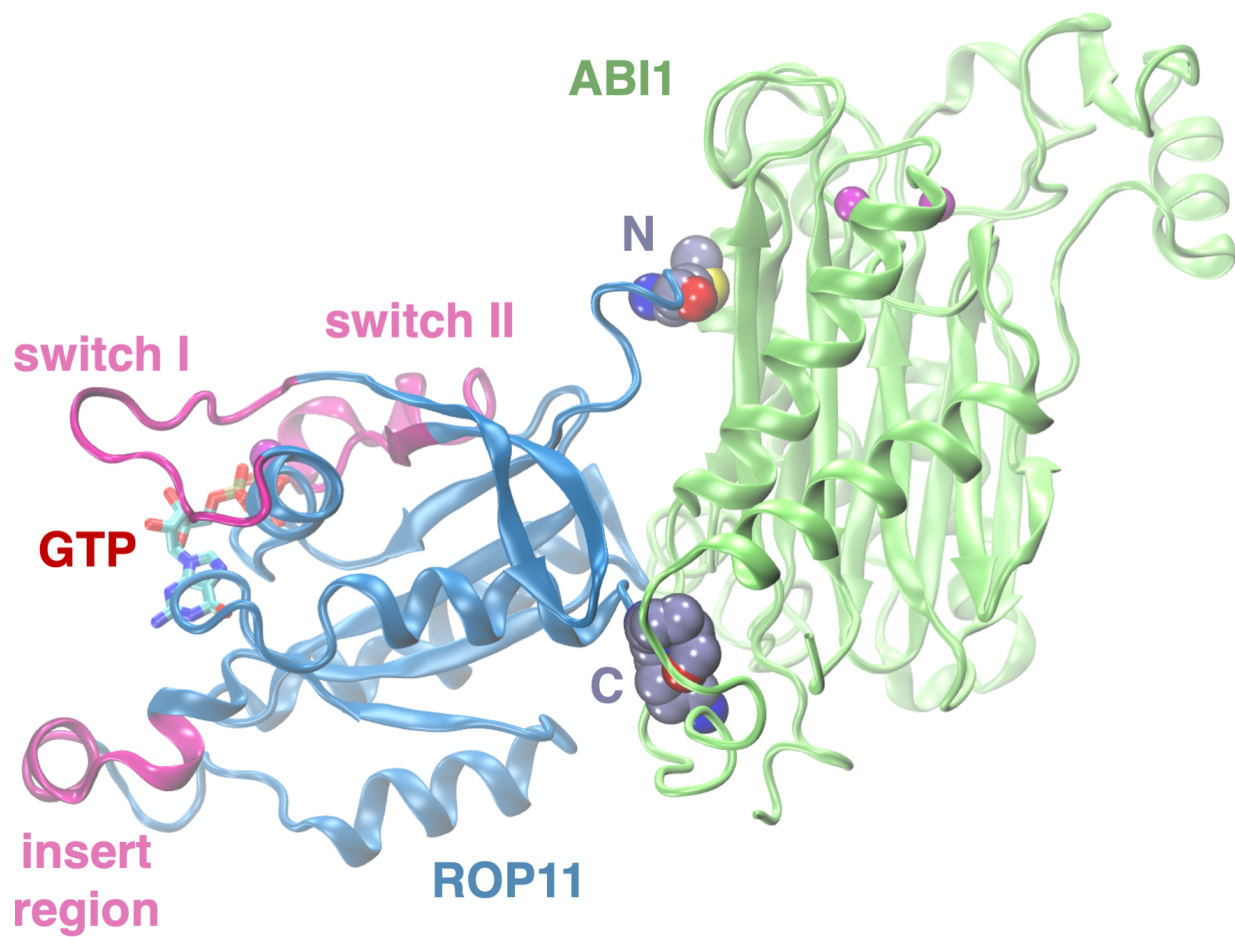


Fig. S13. The candidate complex structure of the state 3 where both N- and C-terminal residues of ROP11 are involved in forming the interface, which is unlikely to be physical.

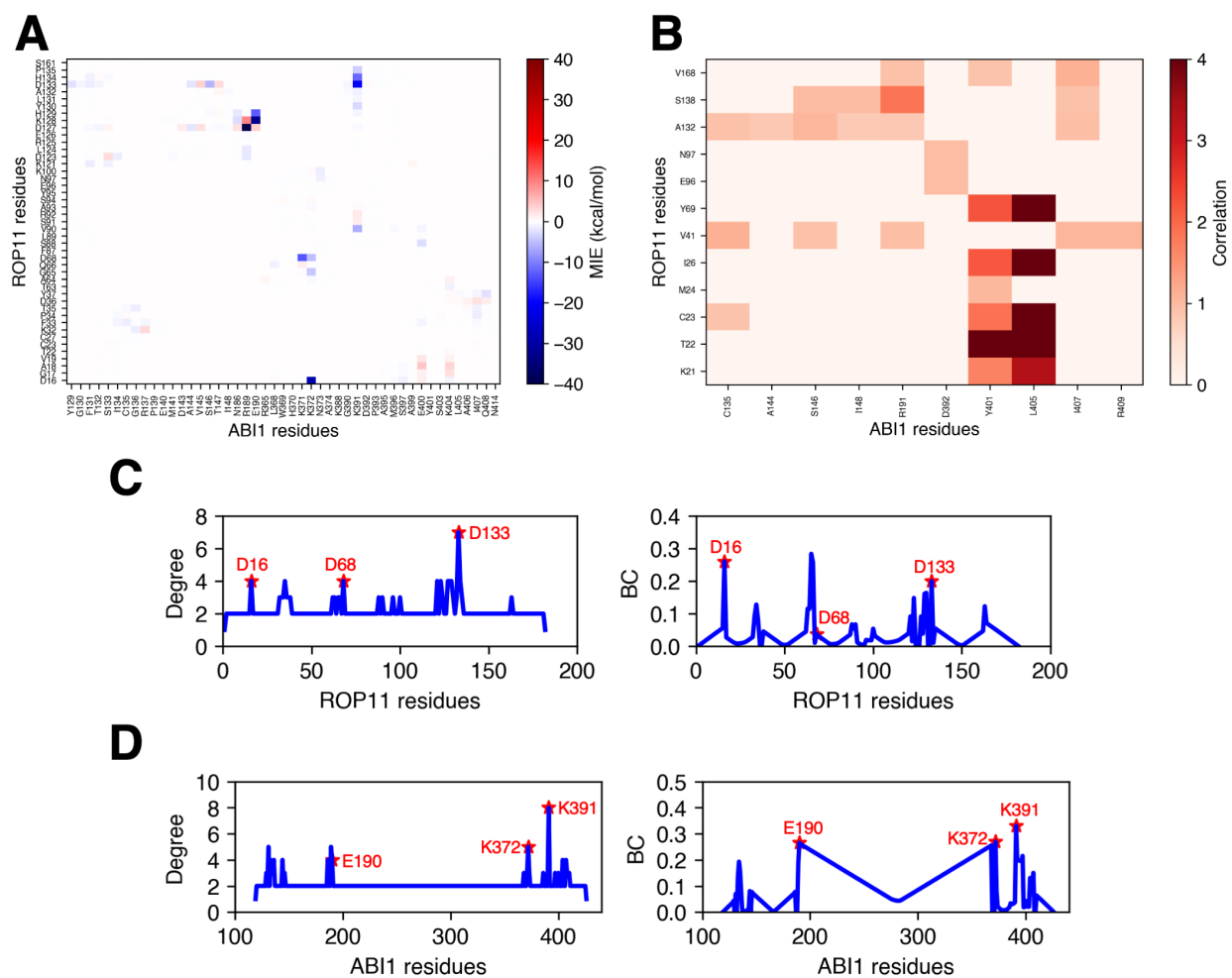


Fig. S14. Identification of critical residue-residue pairs in state 240. (A) Mean interaction energy (MIE) matrix and (B) residue correlation matrix for the residue-residue pairs between ABI1 and ROP11. Network analysis reveals the degree and betweenness-centrality (BC) of the residues in (C) ROP11 and (D) ABI1. The residues in ROP11 and ABI1 with high degree and BC are highlighted.

References

- [1] T. Schwede, *Nucleic Acids Research*, 2003, **31**, 3381–3385.
- [2] F.-F. Soon, L.-M. Ng, X. E. Zhou, G. M. West, A. Kovach, M. H. E. Tan, K. M. Suino-Powell, Y. He, Y. Xu, M. J. Chalmers, J. S. Brunzelle, H. Zhang, H. Yang, H. Jiang, J. Li, E.-L. Yong, S. Cutler, J.-K. Zhu, P. R. Griffin, K. Melcher and H. E. Xu, *Science*, 2011, **335**, 85–88.
- [3] K. ichi Kosami, I. Ohki, M. Nagano, K. Furuita, T. Sugiki, Y. Kawano, T. Kawasaki, T. Fujiwara, A. Nakagawa, K. Shimamoto and C. Kojima, *Journal of Biological Chemistry*, 2014, **289**, 28569–28578.
- [4] D. A. Case, I. Y. Ben-Shalom, S. R. Brozell, D. S. Cerutti, T. E. I. Cheatham, V. Cruzeiro, T. Darden, R. Duke, D. Ghoreishi, M. Gilson, H. Gohlke, A. Goetz, D. Greene, R. Harris, N. Homeyer, S. Izadi, A. Kovalenko, T. Kurtzman, T. Lee, S. LeGrand, P. Li, C. Lin, J. Liu, T. Luchko, R. Luo, D. Mermelstein, K. Merz, Y. Miao, G. Monard, C. Nguyen, H. Nguyen, I. Omelyan, A. Onufriev, F. Pan, R. Qi, D. Roe, A. Roitberg, C. Sagui, S. Schott-Verdugo, J. Shen, C. Simmerling, J. Smith, R. Salomon-Ferrer, J. Swails, R. Walker, J. Wang, H. Wei, R. Wolf, X. Wu, L. Xiao, D. York and P. Kollman, *Amber 18*, University of California, San Francisco, CA, 2018.
- [5] R. J. Loncharich, B. R. Brooks and R. W. Pastor, *Biopolymers*, 1992, **32**, 523–535.
- [6] T. Darden, D. York and L. Pedersen, *J. Chem. Phys.*, 1993, **98**, 10089–10092.
- [7] J.-P. Ryckaert, G. Ciccotti and H. J. Berendsen, *J. Comput. Phys.*, 1977, **23**, 327–341.
- [8] S. J. Marrink, H. J. Risselada, S. Yefimov, D. P. Tieleman and A. H. de Vries, *The Journal of Physical Chemistry B*, 2007, **111**, 7812–7824.
- [9] L. Monticelli, S. K. Kandasamy, X. Periole, R. G. Larson, D. P. Tieleman and S.-J. Marrink, *Journal of Chemical Theory and Computation*, 2008, **4**, 819–834.
- [10] Z. Li, J. Kang, N. Sui and D. Liu, *Journal of Integrative Plant Biology*, 2012, **54**, 169–179.
- [11] Z. Li, Z. Li, X. Gao, V. Chinnusamy, R. Bressan, Z.-X. Wang, J.-K. Zhu, J.-W. Wu and D. Liu, *Journal of Integrative Plant Biology*, 2012, **54**, 180–188.
- [12] X. Periole, M. Cavalli, S.-J. Marrink and M. A. Ceruso, *Journal of Chemical Theory and Computation*, 2009, **5**, 2531–2543.
- [13] M. J. Abraham, T. Murtola, R. Schulz, S. Páll, J. C. Smith, B. Hess and E. Lindahl, *SoftwareX*, 2015, **1-2**, 19–25.
- [14] G. R. Bowman, D. L. Ensign and V. S. Pande, *J. Chem. Theory Comput.*, 2010, **6**, 787–794.
- [15] D. Shukla, C. X. Hernández, J. K. Weber and V. S. Pande, *Accounts of Chemical Research*, 2015, **48**, 414–422.
- [16] B. E. Husic and V. S. Pande, *Journal of the American Chemical Society*, 2018, **140**, 2386–2396.
- [17] Y. Naritomi and S. Fuchigami, *J. Chem. Phys.*, 2011, **134**, 065101.
- [18] R. T. McGibbon and V. S. Pande, *J. Chem. Phys.*, 2015, **142**, 124105.
- [19] M. P. Harrigan, M. M. Sultan, C. X. Hernández, B. E. Husic, P. Eastman, C. R. Schwantes, K. A. Beauchamp, R. T. McGibbon and V. S. Pande, *Biophys. J.*, 2017, **112**, 10–15.
- [20] R. T. McGibbon, C. X. Hernández, M. P. Harrigan, S. Kearnes, M. M. Sultan, S. Jastrzebski, B. E. Husic and V. S. Pande, *J. Open Source Software*, 2016, **1**, 00034.
- [21] T. A. Wassenaar, K. Pluhackova, R. A. Böckmann, S. J. Marrink and D. P. Tieleman, *Journal of Chemical Theory and Computation*, 2014, **10**, 676–690.

- [22] Y. Sugita, A. Kitao and Y. Okamoto, *J. Chem. Phys.*, 2000, **113**, 6042–6051.
- [23] J. C. Phillips, R. Braun, W. Wang, J. Gumbart, E. Tajkhorshid, E. Villa, C. Chipot, R. D. Skeel, L. Kale and K. Schulten, *J. Comput. Chem.*, 2005, **26**, 1781–1802.
- [24] M. R. Shirts and J. D. Chodera, *J. Chem. Phys.*, 2008, **129**, 124105.
- [25] H.-J. Woo and B. Roux, *Proc. Natl. Acad. Sci. U.S.A.*, 2005, **102**, 6825–6830.
- [26] J. C. Gumbart, B. Roux and C. Chipot, *J. Chem. Theory Comput.*, 2012, **9**, 794–802.
- [27] J. C. Gumbart, B. Roux and C. Chipot, *J. Chem. Theory Comput.*, 2013, **9**, 3789–3798.
- [28] C. Zhao and D. Shukla, *bioRxiv*, 2019, 721761.
- [29] O. Serçinoğlu and P. Ozbek, *Nucleic Acids Research*, 2018, **46**, W554–W562.